ORIGINAL PAPER

TitaniQ under pressure: the effect of pressure and temperature on the solubility of Ti in quartz

Jay B. Thomas · E. Bruce Watson ·
Frank S. Spear · Philip T. Shemella ·
Saroj K. Nayak · Antonio Lanzirotti

Abstract Quartz and rutile were synthesized from silica-saturated aqueous fluids between 5 and 20 kbar and from 700 to 940°C in a piston-cylinder apparatus to explore the potential pressure effect on Ti solubility in quartz. A systematic decrease in Ti-in-quartz solubility occurs between 5 and 20 kbar. Titanium K-edge X-ray absorption near-edge structure (XANES) measurements demonstrate that Ti^{4+} substitutes for Si^{4+} on fourfold tetrahedral sites in quartz at all conditions studied. Molecular dynamic simulations support XANES measurements and demonstrate that Ti incorporation onto fourfold sites is favored over interstitial solubility mechanisms. To account for the P–T dependence of Ti-in-quartz solubility, a least-squares method was used to fit Ti concentrations in quartz from all experiments to the simple expression

$$RT \ln X_{TiO_2}^{quartz} = -60952 + 1.520 \cdot T(K) - 1741 \cdot P(kbar) \\ + RT \ln a_{TiO_2}$$

where R is the gas constant 8.3145 J/K, T is temperature in Kelvin, $X_{TiO_2}^{quartz}$ is the mole fraction of TiO_2 in quartz and a_{TiO_2} is the activity of TiO_2 in the system. The P–T dependencies of Ti-in-quartz solubility can be used as a thermobarometer when used in combination with another thermobarometer in a coexisting mineral, an independent P or T estimate of quartz crystallization, or well-constrained phase equilibria. If temperature can be constrained within ±25°C, pressure can be constrained to approximately ±1.2 kbar. Alternatively, if pressure can be constrained to within ±1 kbar, then temperature can be constrained to approximately ±20°C.

Keywords Quartz · Titanium · Solubility · Thermobarometry · Thermometry · XANES

J. B. Thomas (✉) · E. Bruce Watson · F. S. Spear
Department of Earth and Environmental Sciences,
Rensselaer Polytechnic Institute, 110 8th St.,
Troy, NY 12180, USA
e-mail: thomaj2@rpi.edu

P. T. Shemella · S. K. Nayak
Department of Physics, Applied Physics, and Astronomy,
Rensselaer Polytechnic Institute, Troy, NY 12180, USA

A. Lanzirotti
National Synchrotron Light Source, Brookhaven National
Laboratory, The University of Chicago—CARS, Upton,
NY 11973, USA

Introduction

The widespread occurrence of quartz in crustal rocks attests to its stability over a wide range of P–T conditions. Until recently, it was not widely recognized that the trace element geochemistry of quartz could provide quantifiable information regarding the crystallization conditions of rocks. Although many studies have shown that trace elements are sparingly soluble in quartz (Ti, Al, Fe, etc.; Denen 1964, 1966; Suttner and Leininger 1972; Sprunt 1981; Moneke et al. 2002; Müller et al. 2003; Landtwing and Petke 2005; Rusk et al. 2006), there are few studies that have attempted to quantify trace element solubility behavior in quartz. Experiments conducted over a range of temperatures at 10 kbar were recently used to calibrate the temperature dependence of Ti-in-quartz solubility, and results were presented as a Ti-in-quartz (TitaniQ) thermometer (Wark and Watson 2006).

Thermometers based on Ti in quartz, Zr in rutile (TiO_2) and Ti in zircon ($ZrSiO_4$) were originally calibrated at 10 kbar, and the effect of pressure on the thermometers was evaluated in only a few experiments (Watson et al. 2006;

Wark and Watson 2006). Initial applications of the TitaniQ thermometer to several geologic systems suggested that the pressure effect on relevant solubilities was low because temperatures returned from the thermometers were consistent with other thermometric methods (Wark and Watson 2006; Wark et al. 2007; Wiebe et al. 2007). However, there are several reports in which the 10 kbar TitaniQ calibration returned temperatures that are irreconcilable with phase equilibria and other thermometric constraints on crystallization temperature (Lowers et al. 2007; Ghisoro and Evans 2008, p 1020). Ostapenko et al. (2007) predicted a pressure effect on Ti solubility in quartz based on experiments conducted at 2 kbar (Ostapenko et al. 1987). Subsequent experimental investigation into the Zr-in-rutile thermometer (Tomkins et al. 2007) revealed that Zr-in-rutile solubility is modestly dependent on pressure due to differences in size between Zr^{4+} (0.72 Å) that replaces Ti^{4+} (0.61 Å) on the sixfold Ti site in rutile. The pressure effect on substitution of Zr^{4+} for Ti^{4+} in sphene is larger than that for rutile and was utilized to develop the Zr-in-sphene thermobarometer (Hayden et al. 2007).

An outstanding question is as follows: how does pressure affect Ti-in-quartz solubility and the TitaniQ thermometer? The Zr-in-rutile and Zr-in-sphene solubilities are decreased with increasing pressure because substitution of the $\sim$15% larger Zr^{4+} for Ti^{4+} on sixfold coordinated sites in compressed crystal structures becomes unfavorable at high pressure. There are limited experimental and empirical data that have explored the pressure effect on the Ti-in-zircon thermometer (Ferry and Watson 2007). Combined quantum mechanical simulations and Monte-Carlo calculations suggest diminished Ti solubility in zircon at ultrahigh pressures. At pressures relevant to most crustal settings Ti substitutes for Si, but with increasing pressure Ti siting increasingly favors the eightfold Zr site in the zircon structure (Ferris et al. 2008). It is expected that pressure will affect Ti-in-quartz solubility because there is an $\sim$38% size difference between Ti^{4+} that replaces tetrahedrally coordinated Si^{4+} in the quartz structure, and among silicate minerals quartz is anomalously compressible (e.g., Levien et al. 1980). The original TitaniQ calibration can be used to accurately determine quartz crystallization temperature for pressures near 10 kbar. However, successful application of the Ti-in-quartz thermometer at other pressures depends upon how strongly pressure affects Ti solubility in quartz.

In this study we present new data on Ti-in-quartz solubility obtained from experiments conducted from 5 to 20 kbar extending the range of conditions explored during calibration of the TitaniQ thermometer (Wark and Watson 2006). Titanium activity of all experiments was fixed at unity by co-crystallization of rutile and quartz so that the effect of pressure on Ti-in-quartz solubility could be

specifically investigated. Titanium K-edge X-ray absorption near-edge structure measurements were conducted to evaluate the substitution mechanism responsible for Ti incorporation into quartz over the range of experimental conditions. We present a simple model that can be used to predict P–T dependencies of Ti-in-quartz solubility up to $\sim$20 kbar. The P–T dependencies of Ti-in-quartz solubility can be used as a thermobarometer when used in combination with another thermobarometer in a coexisting mineral (e.g., Zr-in-rutile) or an independent P or T estimate of quartz crystallization.

Methods

Quartz, rutile and zircon were grown from silica-saturated aqueous fluids in the SiO_2-TiO_2-ZrO_2 system (Fig. 1) in a piston-cylinder apparatus at pressure between 5 and 20 kbar and temperatures ranging from 700–940°C (Table 1). Starting materials TiO_2 (anatase; Alfa Aesar), ZrO_2 (Alfa Aesar), distilled H_2O and either quartz powder (<22 μm; Brazil quartz) or SiO_2 glass (Alfa Aesar) were added to silver capsules ($\sim$0.5 cm^3). Capsules were sealed during cold pressurization of each experiment. Standard 19-mm-diameter piston-cylinder assemblies with crushable materials were used for all experiments (Fig. 2). Temperature was monitored by type-C thermocouples ($W_{97}Re_3$–$W_{75}Re_{25}$); reported temperatures (Table 1) are believed to be accurate to within $\sim$5°C considering the small uncertainty in T measured at the thermocouple in addition to the larger one arising from T differences across the capsule (see "Results and Discussion" section). In experiments at
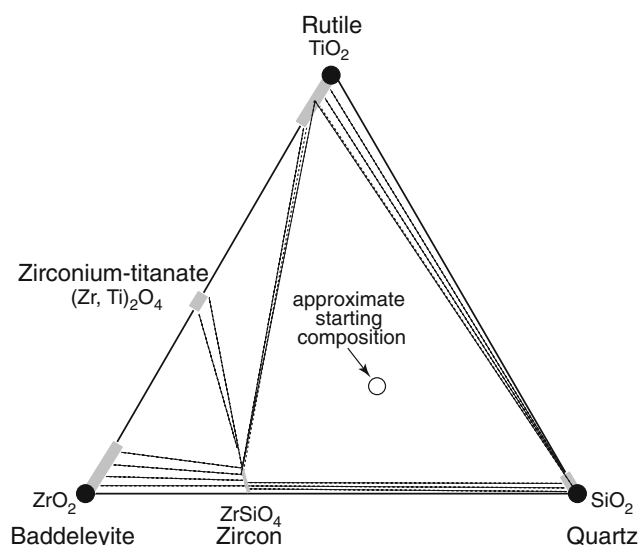

Fig. 1 Ternary diagram of the TiO_2-ZrO_2-SiO_2 system after Tomkins et al. (2007) and Tailby et al. (2010) showing the approximate starting composition. All experiments contained quartz, rutile and zircon

Table 1 List of experimental run conditions and results

Run #	T (°C)	P (kbar)	Time (h)	Ti (ppm)	Standard error[a]	$X_{TiO_2}^{Quartz} \times 10^{-4}$	Standard error $\times 10^{-6}$
QTiP-38	800	5	54	380	8 (11)	4.771	10.23
QTiP-39	900	5	25	813	5 (12)	10.21	5.674
QTiP-41	725	5	48	274	3 (14)	3.440	4.175
QTiP-19	900	10	68	307	2 (14)	3.852	2.385
QTiP-4	800	15	47	38	6 (17)	0.477	7.093
QTiP-6	900	15	92	103	5 (12)	1.298	6.351
QTiP-7	700	15	80	18	1 (26)	0.223	0.816
QTiP-10	940	15	120	167	5 (24)	2.100	6.035
QTiP-11	875	15	142	96	5 (19)	1.211	6.060
QTiP-12	775	15	120	40	2 (15)	0.502	2.088
QTiP-25	750	15	120	28	1 (27)	0.353	1.358
QTiP-26	825	15	116	56	2 (27)	0.707	2.193
QTiP-1	900	20	117	63	4 (8)	0.796	4.369
QTiP-13	875	20	112	46	1 (18)	0.577	1.556
QTiP-14	940	20	120	100	2 (22)	1.250	2.378
QTiP-15	800	20	120	16	2 (13)	0.201	2.337
QTiP-16	775	20	115	21	2 (10)	0.267	1.974
QTiP-17	850	20	120	49	2 (14)	0.609	2.200
QTiP-29	825	20	115	24	<1 (25)	0.306	0.472

[a] Values in parentheses are the number of analyses

$P \geq 10$ kbar, the reported pressures are believed be accurate within ± 200 bars based on previous calibrations in our laboratory of similar NaCl-Pyrex-MgO assemblies (see Fig. 2) at pressures of 8 kbar and higher. The 5-kbar experiments may have a somewhat larger pressure uncertainty of ± 500 bars because the crushable materials in the pressure cell (Fig. 2) may not have been fully compacted during the experiments. Experiments were run for 1–5 days and quenched to below 100°C within 20 s by turning off the furnace power. Four experiments were conducted at 1 kbar in cold-seal pressure vessels by adding the same starting materials listed above to 3-mm-diameter Pt capsules that were welded closed.

Upon opening capsules, water was always present at the end of experiments. Single crystals of quartz were removed from capsules and mounted in epoxy and polished prior to analysis by electron microprobe. Cathodoluminescence (CL) imaging and spectroscopy were used to characterize trace element distributions in quartz crystals using a Gatan MonoCL attached to an electron microprobe (Wark and Spear 2005; Rusk et al. 2006; Spear and Wark 2009). Most CL images were collected in panchromatic mode using a 10 nA beam current and 15 kV accelerating voltage. Quantitative Ti analyses were made at RPI using a Cameca SX-100 electron microprobe equipped with five wavelength dispersive spectrometers containing oversized (22 × 60 mm) diffraction crystals to facilitate trace element quantification. Standardization on rutile and quartz
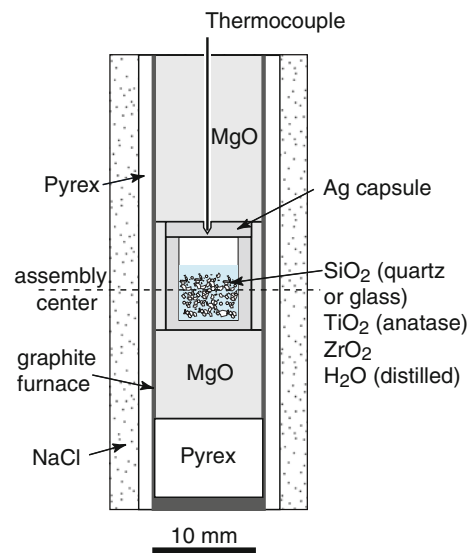

Fig. 2 Piston-cylinder assembly used in all experiments

was performed at 20 nA to avoid pulse-height analyzer peak shifts that accompany high count rates. A beam current of 200 nA and 15 kV accelerating voltage was used for analyses. The Ti $K\alpha$ X-rays were simultaneously counted on four spectrometers (400 s peak, 200 s background) yielding a detection limit of ~ 8 ppm. Silicon $K\beta$ X-rays were counted to verify that the analyzed material was indeed SiO_2. Replicate analyses of a standard silicate

mineral with 2,640 ppm Ti yielded a standard error of ~ 6 ppm.

Ti K-edge X-ray absorption near-edge structure (XANES) spectra were measured on beamline X-26A at the National Synchrotron Light Source at Brookhaven National Laboratory to probe the local coordination environment around Ti ions in the experimentally grown quartz crystals. In order to maximize the count rate, quartz crystals from the highest temperature experiments (e.g., highest Ti concentration) from each pressure series were selected for analysis (runs 10, 14 19 and 39; Table 1). A detailed description of beamline components, parameters and typical operating conditions can be found at (http://www.bnl.gov/x26a/). Only a brief description of details related specifically to our analyses is given below.

The X-26A X-ray microprobe was operated in monochromatic, focused mode using Kirkpatrick-Baez geometry optics that focused the 400×400 μm beam down to ~ 6–10 μm. The beam was monochromatized with a channel-cut (111) silicon crystal located 6 m from the source and cooled to 11°C. A Radiant Vortex-EX silicon drift single element detector was located in the storage ring plane at 90° to the incident beam, and fluorescence was recorded at 45° to the sample. The beamline at X-26A is capable of conducting XANES measurements with an ~ 10–100 ppm detection limit (lowest concentration measured here is ~ 100 ppm). Titanium foil was used to calibrate the detector at 4,966 eV, and repeat measurements of the Ti foil were used to check the calibration throughout the analytical session. Over the 24-h period during which spectra were collected the monochromator energy calibration changed by <0.2 eV. Spectra were recorded using steps of 5 (4,910–4,960 eV), 0.2 (4,960–4,986 eV) and 2 eV (4,987–5,050 eV) with dwell times adjusted to accumulate a total of $>10^4$ counts. The spectral data were normalized to account for differences in Ti concentrations between samples, detector and amplifier settings, etc., using Athena software (Ravel and Newville 2005). Normalization was achieved by fitting a line to the data in the pre-edge energy range and regressing a polynomial through the data in the post-edge energy range, and background absorption was removed. The goodness of fit was evaluated 'by eye', and Athena input parameters were adjusted so that regressions passed through the middle of the raw spectral data.

Density functional theory calculations (DFT) were performed to computationally investigate Ti incorporation into quartz as a function of pressure. Simulations were performed using the generalized gradient approximation functional PBE (Perdew et al. 1996) with a plane wave basis set (Kresse and Furthmuller 1996; Paier et al. 2005), implemented with CPMD code (IBM Corporation), and utilizing the IBM BG/L architecture (Andreoni and Curioni

2000; Bekas and Curioni 2008). Wave function optimization was sampled at the Γ point in the Brillouin zone. Full structural relaxation was performed at each simulated pressure (e.g., lattice constant) for pure quartz and quartz containing Ti with Troullier–Martins pseudopotentials (Troullier and Martins 1991) and an electronic kinetic energy cutoff of 80 Ry. Similar computational methods have been successfully used for SiO_2 systems (Zicovich-Wilson et al. 2004). In order to compare energies between systems with different lattice constants, the cutoff was increased to above the plane wave convergence point, 270 Ry for this system. With this cutoff, the electronic wave function was found and the single point energy was calculated at every geometry, and each structure was found to have negligible ionic forces.

Results and discussion

Experimental run conditions and Ti concentrations of synthesized quartz crystals are listed in Table 1. All experiments were conducted in the SiO_2-TiO_2-$ZrSiO_4$ field of the TiO_2-ZrO_2-SiO_2 system (Fig. 1) with the stable equilibrium assemblage composed of quartz, rutile and zircon, which buffered SiO_2, TiO_2 and $ZrSiO_4$ activities at their maximum possible values. Run products typically consisted of large (~ 1 mm), euhedral quartz crystals (Fig. 3a) that nucleated and grew from the capsule lid along with fine-grained rutile, zircon and amorphous silica (optically isotropic) that was dissolved in the aqueous fluid during the experiment. Quartz crystals typically contained rutile and zircon inclusions (Fig. 3b, c) confirming co-crystallization of quartz and rutile. Offsetting the capsule ~ 1–1.5 mm above the center of the piston-cylinder assembly (Fig. 2) introduced a small thermal gradient (Watson et al. 2002) that caused large single crystals of quartz to grow from the slightly cooler capsule lid (Fig. 3). Although the quartz grows in a small thermal gradient, its crystallization temperature is very well constrained to within 2°C because the quartz always grew on the capsule lid <1 mm away from the thermocouple. The formation of large single crystals allowed us to simply remove the crystals from the fine-grained rutile thereby avoiding secondary fluorescence problems that frustrated previous studies in which fine-grained quartz and rutile were intimately mixed (Watson et al. 2006; Wark and Watson 2006). Any rutile adhered to quartz surfaces was simply removed by polishing, and quartz analyses were conducted at distances >200 μm from any rutile inclusions.

Prior to measuring Ti in quartz, CL was used to image each crystal. Several CL spectroscopic measurements confirmed that the light emitted from the samples during electron beam irradiation was in the 415 nm (blue) region,

Fig. 3 Images of experimentally grown quartz. a Large single crystal of quartz showing well-developed external morphology. b Image of quartz showing variable cathodoluminescence intensity, but electron microprobe analyses show relatively uniform Ti concentrations. c Transmitted light photomicrograph of a single crystal of quartz containing rutile and zircon inclusions confirming co-crystallization. d Cathodoluminescence image of quartz that preserves β-quartz external form and shows differences in CL intensity that correlate with measured Ti content
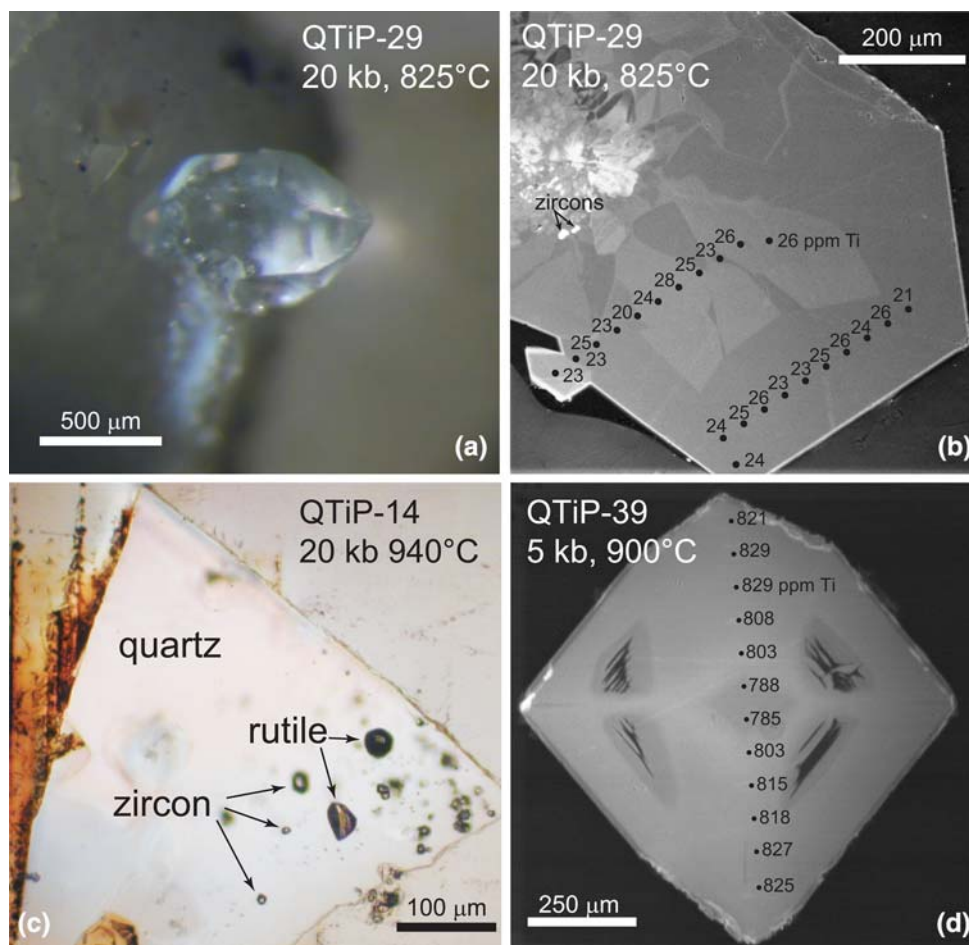
and CL intensity at this wavelength is generally proportional to Ti concentration (Wark and Spear 2005; Rusk et al. 2006; Spear and Wark 2009). The brightest CL regions of quartz crystals correlated with relatively higher Ti contents, compared to darker CL regions, and served as a guide to pick spots for quantitative Ti analyses. Cathodoluminescence images reveal that most quartz crystals have relatively uniform Ti concentrations (Fig. 3b, d).

In the low pressure cold-seal experiments in which powdered quartz was used as the starting material, the crystals did not coarsen enough to allow accurate electron probe analyses of the thin overgrowth rims (<2 μm). For cold-seal experiments in which silica glass was used as starting material, large masses of polycrystalline material (~ 2 mm) formed during the experiments. Because Raman microprobe measurements showed that the polycrystalline material is a mixture of metastable cristobalite and tridymite, the 1-kbar experiments are not further considered here.

Thermodynamic analysis

When quartz crystallizes in the presence of rutile, Ti solubility in quartz is governed by the equilibrium

$$TiO_2^{rutile} = TiO_2^{quartz}. \tag{1}$$

The equilibrium constant for this reaction is

$$K = \frac{a_{TiO_2}^{quartz}}{a_{TiO_2}} \tag{2}$$

where a_i is the activity of component i. Since rutile is present in all experiments, $a_{TiO_2} = 1$ and the equilibrium constant is $K = a_{TiO_2}^{quartz}$. The low Ti concentrations found in experimental and natural quartz crystals (Table 1), justifies the assumption that $a_{TiO_2}^{quartz} \approx k X_{TiO_2}^{quartz}$, where k is the Henry's Law coefficient and $X_{TiO_2}^{quartz}$ is the mole fraction of TiO_2 in quartz (see "Appendix" for equation to convert Ti (ppm) to $X_{TiO_2}^{quartz}$).

At equilibrium,

$$\Delta \overline{G}^{\circ} = \Delta \overline{H}^{\circ} - T(\Delta \overline{S}^{\circ} - R \ln k_{TiO_2}) + P \Delta \overline{V}^{\circ}$$
$$+ RT \ln X_{TiO_2}^{quartz} - RT \ln a_{TiO_2} = 0 \tag{3}$$

in which a_{TiO_2} is the activity of TiO_2 in the system. The TiO_2 endmember in Eq. 3 is fictive TiO_2 in the quartz structure having regular solution properties at low concentrations into the Henry's Law limit. Making substitutions and rearranging gives

$$\ln X_{\text{TiO}_2}^{\text{quartz}} = \frac{-\Delta \overline{H}^\circ + T\Delta \overline{S}^\circ - P\Delta \overline{V}^\circ + RT \ln a_{\text{TiO}_2} - RT \ln k}{RT},$$

(4)

which predicts that Ti solubility in quartz, $X_{\text{TiO}_2}^{\text{quartz}}$, will vary with P and T. In simple terms, the temperature dependence of $\ln X_{\text{TiO}_2}^{\text{quartz}}$ is a function of $\Delta \overline{H}^\circ$ (i.e., it is the slope on a plot of $\ln X_{\text{TiO}_2}^{\text{quartz}}$ vs. $1/T$) and $\Delta \overline{S}^\circ$ controls the slopes of isopleths in P–T space.

In the equilibrium defined by Eq. 1 substitution of Ti^{4+} for Si^{4+} is implicit, but the site on which Ti resides in the quartz structure is not specified. It is conceivable that Ti may reside on tetrahedral sites or it may dissolve into interstitial sites, and, thermodynamic variables are unique for each solubility mechanism.

Wark and Watson (2006) experimentally investigated Ti solubility in quartz along a single isobar (10 kbar) to develop the Ti-in-quartz thermometer. The effect of pressure on the TitaniQ thermometer was not pursued because its application to natural quartz crystals from several geologic systems, the temperatures returned from TitaniQ were in general agreement with estimates determined from other methods (e.g., Fe–Ti thermometry from the Bishop Tuff, cf. Wark et al. 2007). For this reason, the $\Delta \overline{V}^\circ$ term in Eq. 3 was believed to be sufficiently small that the 10 kbar calibration of the TitaniQ thermometer could be applied to quartz crystallized at other pressures.

The new experimental results for Ti-in-quartz solubility at 5, 10, 15 and 20 kbar are shown in Fig. 4 along with the 10-kbar data of Wark and Watson (2006). Linear fits to the data on $\ln X_{\text{TiO}_2}^{\text{quartz}}$ vs. $1/T$ plots show that isobars are subparallel to one another with slopes that increase with increasing pressure:
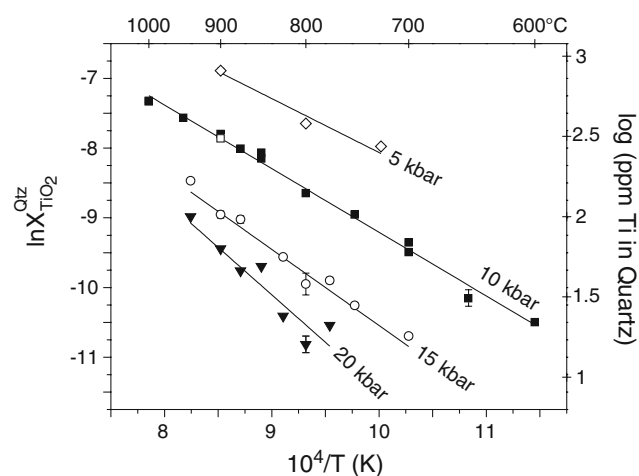

Fig. 4 Ti concentrations in experimentally grown quartz plotted against $1/T$. All 10 kbar results, except for the open symbol, are from Wark and Watson (2006). The lines are least-squares fits to the data. Uncertainties are smaller than symbols unless shown by *error bars*

$$5\,\text{kbar}: \ln X_{\text{TiO}_2}^{\text{Quartz}} = -1.44(\pm 1.39) - \frac{6541(\pm 1429)}{T(K)}$$

$$R^2 = 0.91$$

(5)

$$10\,\text{kbar}: \ln X_{\text{TiO}_2}^{\text{Quartz}} = -0.08(\pm 0.2) - \frac{9132(\pm 219)}{T(K)}$$

$$R^2 = 0.99$$

(6)

$$15\,\text{kbar}: \ln X_{\text{TiO}_2}^{\text{Quartz}} = 0.53(\pm 0.37) - \frac{10991(\pm 405)}{T(K)}$$

$$R^2 = 0.99$$

(7)

$$20\,\text{kbar}: \ln X_{\text{TiO}_2}^{\text{Quartz}} = 4.03(\pm 1.3) - \frac{15784(\pm 1475)}{T(K)}$$

$$R^2 = 0.95$$

(8)

which have the form expected on the basis of the simple thermodynamic relationship described by Eq. 3. The quoted uncertainties in the linear regressions are at the 2σ level and fits considered uncertainties only in measured Ti contents because temperature uncertainties are relatively small.

The 5-, 10- and 15-kbar isobars have relatively even spacing in $\ln X_{\text{TiO}_2}^{\text{quartz}}$ vs. $1/T$ space, but the linear fit to data along the 20-kbar isobar has a steeper slope and lies closer to the 15-kbar isobar than would be expected based on spacing between lower pressure isobars (Fig. 4). There is some scatter of the data, especially at the low temperature end of the 20-kbar isobar as the Ti concentrations approach the analytical detection limit of the electron microprobe (~ 8 ppm Ti), but solubilities at this pressure clearly deviate from the linear trend of decreasing solubility with increasing pressure as defined by the 5-, 10- and 15-kbar isobars. The deviation from constant spacing between the isobars is especially evident at the high temperature end of the 20-kbar isobar shown in Fig. 4.

Although linear fits to each isobaric series accurately predict the temperature dependence of Ti solubility in quartz at a given pressure, such simple fits cannot account for the strong solubility dependence upon pressure. The experimental data can be simultaneously fit using a least-squares approach to quantify the dependencies of Ti solubility on both P and T. It is important to note that the fit parameters obtained from least-squares fits are only relevant for a single solubility mechanism. As such, prior to calibrating a Ti-in-quartz thermobarometer, we must first characterize Ti siting in the quartz crystals synthesized over the range of pressures investigated.

X-ray-absorption near-edge structure: a direct probe of the Ti coordination environment

There are several possible mechanisms by which Ti may enter the quartz structure. Equation 1 describes Ti

incorporation into quartz, but it does not specify where in the quartz structure Ti resides. If one solubility mechanism prevails at all pressures, then a single set of fit parameters that describe P–T dependencies of Ti-in-quartz solubility can be extracted from least-squares fits to all the experimental data. Perhaps the simplest solubility mechanism involves substitution of Ti^{4+} for Si^{4+} on tetrahedral sites that are coordinated by four oxygens. However, other more complex solubility mechanisms are conceivable and it is not known whether pressure affects Ti siting (e.g., Ferris et al. 2008). Solubility mechanisms that involve incorporation of Ti^{4+} onto interstitial sites with variable coordination (i.e., $N > 4$), $Ti^{3+} + H^+$ substitution for Si^{4+}, or more complicated coupled substitutions would complicate an experimental P–T calibration for a Ti-in-quartz thermobarometer and must be considered.

XANES measurements directly probe the geometry of Ti-oxygen polyhedra and can provide information on the local coordination environment. The Ti near-edge region from 4,960 to 5,020 eV has up to nine resolvable absorption features due to variations in Ti-site geometry. Of these features, the Ti pre-K-edge absorption at $\sim 4{,}969$ eV undergoes the largest changes in position and normalized height as a function of Ti coordination and valence (Fig. 5a; Waychunas 1987; Farges et al. 1996a, b, 1997; Farges 1997; Berry et al. 2007; Tailby et al. 2010). Increasing Ti coordination from four to five to six nearest oxygen neighbors results in a significant decrease in pre-edge peak intensity and shifts the pre-edge feature position to higher energies. XANES spectra of experimentally grown quartz crystals and rutile standard materials were compared to previously characterized materials that contain Ti in four-, five- and sixfold coordination (Fig. 5b). Measurements of $\alpha - Ti_2^{3+}O_3$ with corundum structure were also made to evaluate the possibility that trivalent Ti was incorporated into the quartz structure.

The octahedral bonding arrangement of Ti^{4+} in rutile produces seven spectral features in Ti K-edge XANES spectra (Fig. 5a). The pre-edge features are attributed to transitions from Ti 1 s energy levels to bound Ti 3d orbitals. There are various explanations for the three pre-edge features observed in spectra of rutile, but all generally involve p orbitals of the Ti absorber site mixing with d orbitals of neighboring Ti ions. The first weak feature at $\sim 4{,}969$ eV has been attributed to quadrupolar transitions to t_{2g} levels of the TiO_6 octahedron. The second pre-edge feature at 4,971.3 eV is attributed to 1s to 3d dipolar transitions to the t_{2g} orbital of the neighboring octahedron adjacent to the Ti absorber site. The third pre-edge feature at $\sim 4{,}974$ eV is attributed to a second dipolar transition of the e_g orbital of neighboring octahedron. The observed feature on the steeply sloping main edge at $\sim 4{,}980$ eV and the first shoulder on the absorption edge at $\sim 4{,}985$ eV are
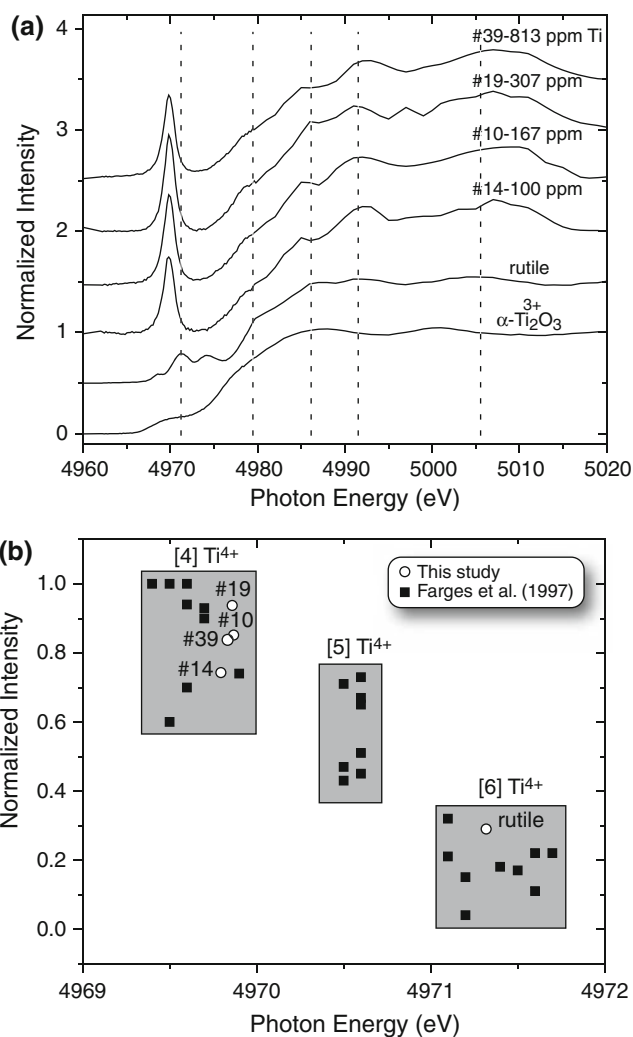

Fig. 5 a Titanium K-edge X-ray absorption near-edge structure spectra of quartz crystals synthesized at 5–20 kbar, a rutile crystal and $\alpha - Ti_2^{3+}O_3$ with corundum structure. The pre-edge feature at $\sim 4{,}969.8$ eV of quartz crystals is larger and shifted to lower energies than that of rutile at $\sim 4{,}971.3$ eV. The vertical dashed lines are visual cues to the approximate positions of spectral features in rutile. Spectral data were normalized to account for differences in samples and detector settings (see "Methods" section). Spectra are vertically offset for clarity. **b** Normalized intensities of pre-edge features that occur between 4,970 and 4,972 eV versus energy position showing fields defined by materials from Farges et al. (1997) that contain Ti^{4+} in fourfold- (IV), fivefold- (V) and sixfold coordination (VI)

attributed to 1s to 4p transitions (Bair and Goddard 1980) and multi-scattering contributions from neighboring ions that reside up to ~ 15 Å from the absorbing Ti site (Farges et al. 1997). Two broad features at $\sim 4{,}992$ and $\sim 5{,}005$ eV are generally unassigned.

As found in previous studies of materials that contain Ti^{4+} in fourfold coordination, Ti K-edge XANES spectra of experimentally grown quartz crystals have up to seven resolvable spectral features, several of which are distinct from those observed in spectra of rutile (e.g., Waychunas

1987; Farges et al. 1997). The most prominent difference between XANES spectra of quartz and rutile occurs in the pre-edge region near $\sim$4,970 eV (Fig. 5a). The pre-edge feature in spectra of quartz crystals is comprised of a single peak that is more intense and shifted to lower energies than the multiple pre-edge features observed for rutile. The increase in intensity of the pre-edge features observed in spectra of compounds that contain fourfold Ti^{4+} has been attributed to the degree of d-p orbital mixing and associated Ti absorber site distortion (Waychunas 1987). Compared to rutile, the feature on the steeply sloping main edge and the first shoulder are also shifted to lower energies by $\sim$1–2 eV, and the broad unassigned features on the main edge generally occur at higher energies (Fig. 5a).

The normalized pre-edge peak intensities of Ti-bearing quartz crystals are significantly higher than the pre-edge feature intensities of rutile, in which Ti^{4+} is coordinated by six oxygens (Fig. 5a). The normalized pre-edge intensities of our quartz crystals range from 0.74 to 0.94, which is comparable to the pre-edge intensities previously measured in reported materials that contain Ti in fourfold coordination (Fig. 5b; Farges et al. 1996a, b, 1997; Farges 1997). The pre-edge feature intensity of rutile measured here is $\sim$0.29, which is also similar to intensities measured for rutile and other materials in which Ti is in sixfold coordination. A second notable difference between the spectra is that the position of the pre-edge peak of our quartz crystals is located at a lower energy than the pre-edge feature of rutile (Fig. 5a, b). Quartz crystals have pre-edge peak positions at $\sim$4,969.8 eV and the pre-edge feature of our rutile is at 4,971.3 eV, positions that are in agreement with previous studies of materials in which Ti^{4+} is in four- and sixfold coordination, respectively (Fig. 5b).

Trivalent Ti is common in lunar and meteoritic minerals, but it is exceptionally rare in terrestrial systems because highly reducing conditions are required (Anderson et al. 1970). It is unlikely that Ti^{3+} was stabilized in our experimental system because the intrinsic oxygen fugacity in our piston-cylinder pressure cells is close to $\sim$FeO-Fe_3O_4. In agreement with previous studies, Ti K-edge XANES spectra of α-Ti_2O_3 that contains Ti^{3+} are clearly different from those of materials containing Ti^{4+} (Fig. 5a; Waychunas 1987). The pre-edge and main-edge regions in spectra of α-Ti_2O_3 are nondescript, characterized by smooth, broad and poorly resolved features that are shifted by $\sim$1–2 eV to lower energies than the spectral features of the rutile and quartz crystals. A direct comparison to materials that contain Ti^{3+} in fourfold coordination is not possible because standards are not available. Based on existing data, XANES spectra of experimentally grown quartz crystals do not show evidence that Ti^{4+} was reduced to Ti^{3+}.

Density functional theory calculations to evaluate energetics of Ti incorporation in quartz with increasing pressure

The energetics of Ti incorporation into quartz as a function of pressure were computationally evaluated using first-principles density functional theory (DFT). Two simple solubility mechanisms were considered: Ti^{4+} substitution for Si^{4+} on the four-coordinated Si site, and incorporation of Ti onto interstitial sites with variable coordination. First-principles calculations were performed to evaluate the most favorable substitution mechanism as a function of pressure. DFT calculations were run for a pure quartz structure and a quartz structure containing Ti^{4+}.

The computational system was based on the α-quartz crystal structure (Levien et al. 1980) determined at 20 kbar. The unit cell was replicated three times in each direction, and the quartz supercell contained 243 atoms (81 Si, 162 O). Titanium was incorporated into the computational system by replacing a single Si with Ti, and was considered with the same supercell dimension as the pure quartz case. The concentration used in the simulations (one part in 243) is larger than that observed in the experiments and in nature by necessity due to computational limitations on the system size; however, the structural effects of Ti incorporation into quartz should be *generally* applicable.

Lattice constants for both the pure quartz system and the Ti-bearing quartz system were scaled between 98 and 104% of the original value of 14.5086 Å determined at 20 kbar (volume = 2,922.46 Å^3). These compression and expansion values are large and correspond to a wide range of pressures, but the structural and energetic trends are continuous and consistent, even for small deviations in the lattice constant. We have also tested the initial coordinate choice for hysteresis effects by using independent calculations with the 1-atm α-quartz crystal structure (Levien et al. 1980) and decreasing the lattice constant by 1%. In this methodological trial we observed identical structural and energetic results that confirm our computational procedure and conclusions.

To explore the possibility of Ti incorporation into quartz through an interstitial solubility mechanism, a single Ti ion was inserted into several different interstitial sites, each with a different Ti–O polyhedral geometry (i.e., differing coordination). In all cases of interstitial siting, simulations yielded Ti–O and Ti–Si bond distances >2.4 Å; much larger than Ti–O bonds observed in both experimental compressibility studies and in our simulations for tetrahedrally coordinated Ti^{4+}. Accordingly, an interstitial solubility mechanism is not further considered, and modeling was focused on simulating Ti substitution on the Si tetrahedral site. The simulations are in agreement with XANES spectra, which also show that Ti-in-quartz solubility is

dominated by incorporation onto the fourfold tetrahedral site (Fig. 5b).

The effect of pressure on the simulated Ti-bearing and pure quartz structures was evaluated by either increasing or decreasing the 20 kbar starting lattice constant (14.5086 Å) to simulate respective decreases or increases in pressure. The change in lattice constant from 14.79 to 14.21 Å represents a change in pressure from 1 bar to 48.6 kbar, a range of pressures much larger than experimentally investigated, to insure that computational results are continuous throughout the pressure range of interest. Computational structural minimizations for changes in pressure revealed essentially identical energetic responses for the pure quartz and the Ti-bearing quartz systems (Fig. 6a). Both structures respond to changes in pressure in a non-linear fashion. Approximately 450 kJ/mol is needed to compress the structure by 4% (e.g., from a lattice constant of 15.0889 to 14.5086 Å). An additional ∼700 kJ/mol is needed to further compress either structure by 2% from 14.5086 to 14.2184 Å. From *any* pressure, an equivalent compression/expansion results in a non-linear exponential change in energy demonstrating that the structure becomes increasingly resistant to compression with increasing pressure. As previously discussed, this computational result supports the experimental results of higher solubility along the 20-kbar isobar (Fig. 4) than predicted by Eqs. 9 and 10, perhaps because the energetics of structural compressibility are not linear (Fig. 6a).

The energy difference with increasing pressure between the pure quartz structure and the quartz structure containing a Ti ion is shown in Fig. 6b. Computational results demonstrate that less Ti will be incorporated into the quartz structure at relatively higher pressures. The Ti-bearing quartz structure is most stable at the lowest simulation pressure (Fig. 6b). At all pressures, repulsive forces between the relatively larger Ti ion cause the Ti–O average bond length to be ∼10% longer than that of the Si–O bond lengths in the pure quartz structure. As the simulation pressure was decreased, the results show that the average bond length in the simulated Ti-bearing quartz structure increases at a higher rate than average bond length in the pure quartz structure (Fig. 6c). This result demonstrates that the substitutional Ti ion is 'uncomfortably close' to its nearest four oxygen neighbors, which is consistent with the increased energy for the Ti-bearing quartz structure shown in Fig. 6b.

The effect of temperature and pressure on titanium solubility in quartz: calibration of a Ti-in-quartz thermobarometer

XANES measurements and DFT calculations confirm that Ti^{4+} substitutes for Si^{4+} on the tetrahedral site; thus, the P and T dependencies shown in Fig. 4 can be fit to a solubility model that describes Ti-in-quartz solubility at any P
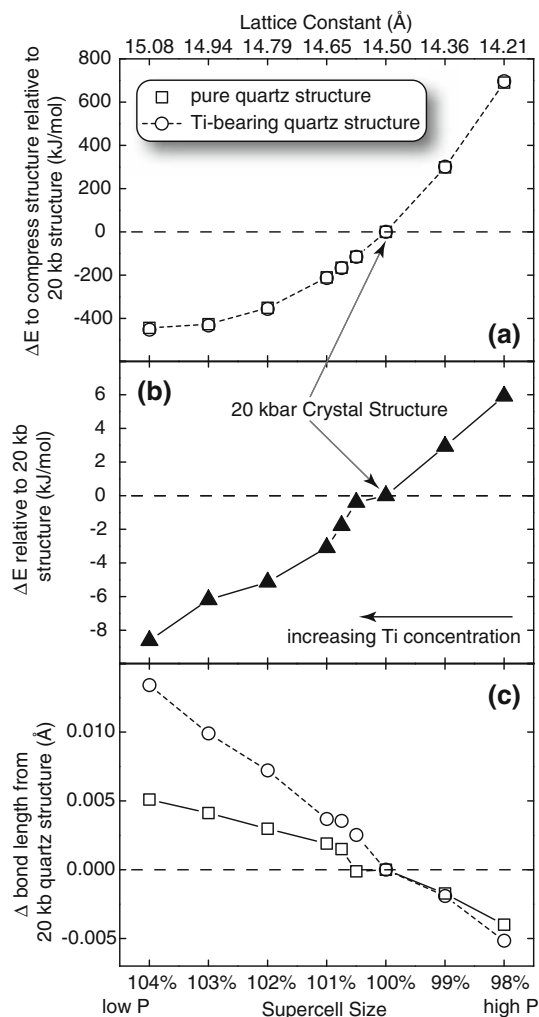

Fig. 6 Results of density functional theory calculations. **a** The change in pure quartz and Ti-bearing quartz system energies relative to the 20 kbar crystal structure. **b** The relative energy of tetrahedrally coordinated Ti in the Ti-bearing quartz structure. **c** The rate of change in the average bond length in the Ti-bearing quartz structure with increasing pressure is higher than that of the pure quartz structure

and T within the range of conditions studied. If the P–T dependencies of Ti-in-quartz solubility are combined with an independent constraint on pressure or temperature, then Ti-in-quartz solubility can be used as a thermobarometer. With this goal in mind, the data from all experiments were simultaneously fit using a least-squares method (Fig. 7) to the polybaric expression

$$RT \ln X_{TiO_2}^{quartz} = -a + b \cdot T(K) - c \cdot P(kbar) + RT \ln a_{TiO_2} \tag{9}$$

in which the adjustable parameters a, b and c are:

$$\begin{aligned} a &= 60952 \pm 3122 \\ b &= 1.520 \pm 0.04 \\ c &= 1741 \pm 63 \end{aligned} \tag{10}$$

and a_{TiO_2} is activity of TiO_2 in the system. The a, b and c terms in Eq. 9 are empirical fit parameters that are related to $\Delta\overline{H}^\circ$, $\Delta\overline{S}^\circ$ and $\Delta\overline{V}^\circ$ in Eqs. 3 and 4. The isobars in $\ln X_{TiO_2}^{quartz}$ vs. $1/T$ space (Fig. 4) show no evidence of curvature suggesting that any change in heat capacity over the range of temperatures investigated is smaller than the uncertainties of the linear fits and thus an adjustable heat capacity term was not included in the polybaric fits (Eq. 9). Ti-in-quartz solubility is characterized by smaller a and b terms and a larger c term than Zr-in-rutile and Zr-in-sphene solubilities (Table 2; Tomkins et al. 2007; Hayden et al. 2007). The strong P–T dependence of Ti-in-quartz solubility is reflected in the magnitude of the b and c terms.

The Ti-in-quartz experiments span the alpha–beta quartz displacive transformation with 21 experiments conducted in the α-quartz stability field and 11 experiments run in the β-quartz stability field. All quartz from the 5-kbar experiments and crystals from eight of the 10-kbar experiments grew in the β-quartz stability field. All other crystals grew in the α-quartz stability field. The data along the 10-kbar isobar provide an opportunity to evaluate potential differences in Ti solubility between α- and β-quartz. There is no indication that the quartz polymorphs have different Ti solubility characteristics—e.g., there is not an obvious inflection along the 10-kbar isobar at the temperature of the α-β transformation (824°C at 10 kbar; Shen et al. 1993). Differences in Ti solubility between α- and β-quartz are not necessarily expected since their structures only differ by low-energy internal rearrangement of bond angles and displacement of atoms. Separately fitting Eq. 9 to quartz that crystallized in the α- and β-quartz stability fields does not substantially change or improve fits to any of the data (see dashed lines in Fig. 7; an offset between dashed lines is present along the 10-kbar isobar because only that data span the α-β quartz transition). Since the fits to experimental data are not significantly improved by separately considering solubilities in the α- versus β- quartz stability fields, we prefer the simple regression of Eqs. 9 and 10 to predict Ti-in-quartz solubility for pressures up to 20 kbar.

Ti-in-quartz solubilities up to 20 kbar are reasonably well constrained by a single set of constant fit parameters. The steeper slope of the 20-kbar isobar data and the change in spacing between the isobars shown on Fig. 4 suggest that Ti-in-quartz solubility behavior may progressively change between $\sim$15 and 20 kbar, perhaps reflecting the anomalous compressibility of quartz and increasing resistance to compression with increasing P (Levien et al. 1980). Given this possibility, the current calibration using Eq. 9 and values listed in Table 2 should not be extrapolated to pressures significantly higher than $\sim$20 kbar. Application of Ti-in-quartz solubility as a thermobarometer to ultrahigh pressure rocks crystallized near the quartz–coesite phase
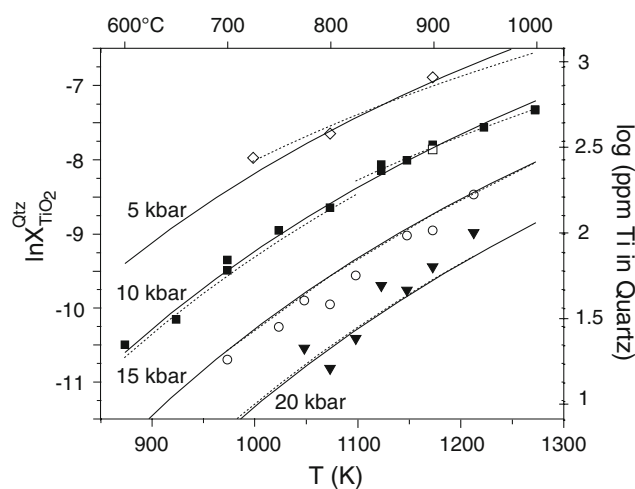

Fig. 7 Least-squares fits to Ti-in-quartz solubilities. *Solid lines* are fits to all the data using Eq. 9. *Dashed lines* are separate fits of Eq. 9 to quartz crystallized in the α- and β-quartz stability fields. See text for details

Table 2 Least-squares fit parameters obtained by fitting Eq. 9 to Ti-in-quartz solubilities shown on Fig. 7, and listed in Table 1 and from Wark and Watson (2006); values for Zr-in-sphene are from fits to data of Hayden et al. (2007)

Parameter	Ti-in-quartz	Zr-in-rutile	Zr-in-sphene
a	60,952 $\pm$ 3,177	85,500 $\pm$ 5	145,943 $\pm$ 5,834
b	1.52 $\pm$ 0.39	29.1 $\pm$ 3	88.9 $\pm$ 6
c	1,741 $\pm$ 63	476 $\pm$ 39	1,538 $\pm$ 128
W[a]	n.a.	10	n.d.

Values for Zr-in-rutile are from Tomkins et al. (2007)

n.a. = not applicable; n.d. = not determined

[a] Tomkins et al. (2007) used an interaction parameter, $W = 10$ kJ/mol, in their equation to fit Zr-in-rutile solubility due to high Zr concentrations in rutile

transformation will require additional experiments at $P > 20$ kbar to further constrain thermodynamic variables.

In a previous study by Ostapenko et al. (1987), quartz and rutile were grown from aqueous solutions in a series of isobaric experiments conducted at 200 bars from 550 to 1,000°C. The Ti concentration in quartz was determined by X-ray diffraction measurements of unit cell parameters. The temperature dependence of Ti concentration in quartz was presented as a geothermometer at 200 bars. Given the differences in experimental and analytical methods, the close agreement between Ti solubility in quartz at 750°C and 200 bars measured by Ostapenko et al. (526 ppm Ti) and values predicted for those conditions using Eq. 9, and values in Table 2 (491 ppm Ti) is remarkable.

Ostapenko et al. evaluated the effect of pressure on Ti solubility in quartz using the $T - X_{TiO_2}^{quartz}$ curve at 200 bars,

and estimations of the molar volume of rutile and the partial molar volume of the TiO_2 component in quartz at several different temperatures. At higher pressures the solubilities extrapolated from the 200 bar experiments of Ostapenko et al. diverge from those measured in our experiments toward higher Ti concentrations. For example, quartz crystals from a 10 kbar and 750°C experiment have 103 ppm Ti (see Table 1 of Wark and Watson 2006) which is similar to the value of 96 ppm predicted from Eq. 9 and values given in Table 2. Based on extrapolations from the isobaric experiments at 200 bars, Ostapenko et al. (2007) predicted a Ti solubility of 207 ppm at 10 kbar and 750°C. The differences between the present study and results of Ostapenko et al. most likely result from inaccuracies associated with estimating the partial molar volume of the Ti component in quartz from isobaric experiments and extrapolating results to pressures significantly higher than their experimental calibration.

Using Ti-in-quartz solubility as a thermobarometer

Potential applications of Ti-in-quartz solubility as a thermobarometer are numerous because quartz is common to most crustal rocks. As long as a_{TiO_2} during quartz crystallization can be reasonably constrained (see calculations of Reid et al. (submitted), and discussions by Wark and Watson 2006, Watson et al. 2006; Wark et al. 2007), P–T dependencies of Ti-in-quartz solubility can be combined with an independent constraint on either P or T to obtain the pressure and temperature of quartz crystallization. Ti-in-quartz solubility can be used to obtain thermobarometric information by several different means, largely dictated by the rock systems that are under consideration. For example, many metamorphic rocks contain rutile and sphene, so the P–T dependencies of Ti-in-quartz solubility can be combined with P–T dependencies of Zr-in-rutile solubility (Tomkins et al. 2007) and/or Zr-in-sphene solubility (Hayden et al. 2007) to estimate pressure and temperature of crystallization. Furthermore, there are numerous other thermometers and barometers based on metamorphic phase equilibria (e.g., Spear 1993, pp. 517–519) that can be used in conjunction with Ti-in-quartz solubility to constrain quartz crystallization conditions. Applying Ti-in-quartz solubility as a thermobarometer in igneous rocks is not as straightforward because most igneous rocks do not contain rutile, and primary unaltered sphene is not always present. Fortunately, well-established melt–solid (e.g., granite melting) and fluid phase equilibria (e.g., fluid inclusions) can be used in conjunction with Ti-in-quartz solubility for thermobarometric applications.

There are practical limitations on applying Ti-in-quartz solubility as a thermobarometer. As discussed earlier, the upper pressure limit for application should be limited to ~20 kbar because of the apparent changes in Ti-in-quartz solubility behavior that occurs at ~20 kbar. Extrapolating our experimental results to higher pressures may yield inaccurate estimates of P–T conditions of crystallization. Lower-temperature applications will be limited by the sensitivity of available analytical techniques. Most modern electron microprobes have lower detection limits of ~10 ppm while laser and ion beam mass spectrometer instruments can achieve detection limits at the 10's of ppb level. The upper temperature limit of applying Ti-in-quartz solubility as a thermobarometer will be limited by the high temperature stability of quartz (e.g., Kennedy et al. 1962). In applying the Ti-in-quartz thermobarometer to high-temperature rocks, one must also bear in mind that diffusion may have modified measured concentrations (cf. Cherniak 2006; Cherniak et al. 2007a, b). Given these considerations and assuming that a_{TiO_2} can be reasonably constrained in rutile-absent rocks, it is likely that Ti-in-quartz solubility will be widely used as a thermobarometer to obtain P–T estimates from rocks that crystallized across the range of conditions shown on Fig. 8.

There are several different ways in which the Ti-in-quartz solubility can be used to obtain P–T estimates of crystallization. Perhaps the most straightforward application of the Ti-in-quartz thermobarometer will be to rocks that contain rutile because a_{TiO_2} will be fixed at unity, and the P–T dependencies of Ti-in-quartz and Zr-in-rutile solubility can be simultaneously used to obtain a crystallization pressure and temperature (Fig. 8a). Although rutile is rare in igneous rocks, it commonly occurs as an accessory mineral in metamorphic rocks. On Fig. 8a, the Ti-in-quartz and Zr-in-rutile isopleths were contoured on a P–T diagram using Eq. 9 and values listed in Table 2. A P–T estimate can be obtained from the intersection of the Ti-in-quartz isopleths with the Zr-in-rutile isopleths. For example, a rock containing 50 ppm Ti-in-quartz and 400 ppm Zr-in-rutile yields crystallization conditions of ~672°C and 9.5 kbar (Fig. 8a). Most rocks will likely yield a range of mineral compositions, so it is essential that careful petrography is used to confirm that the rutile and quartz crystallized contemporaneously—matrix quartz should be paired with matrix rutile and quartz inclusions should be paired with rutile inclusions in the same mineral.

Rocks lacking rutile typically contain another Ti-essential mineral, such as ilmenite ($FeTiO_3$) or sphene ($CaTiSiO_5$), that buffer a_{TiO_2} at values less than one (e.g., Ghent and Stout 1984). According to Eqs. 3, 4 and 9, quartz crystallized at a given P–T condition in systems with $a_{TiO_2} < 1$ will have less Ti than quartz in rutile buffered assemblages. Sphene is a common accessory mineral in igneous and metamorphic rocks. The exact value at which the sphene may buffer a_{TiO_2} depends upon the mineral assemblage present. Figure 8b shows the Ti-in-quartz
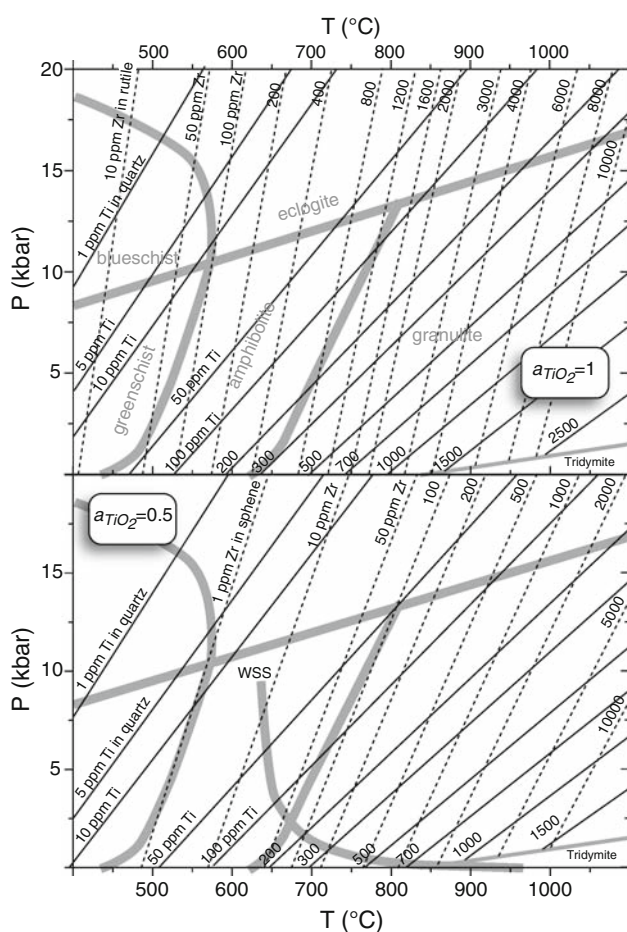
Fig. 8 Isopleths of (**a**) Ti-in-quartz and Zr-in-rutile and (**b**) Ti-in-quartz and Zr-in-sphene. Isopleths were constructed using Eq. 9 and data in Table 2. Approximate metamorphic facies are generalized from Spear (1993) and Philpotts (1990). The curve labeled WSS is the water-saturated solidus for 'minimum' compositions from references listed in Holtz and Johannes (1994)

isopleths and Zr-in-sphene isopleths for $a_{TiO_2} = 0.5$ contoured on a *P–T* diagram using Eq. 9 and values listed in Table 2. The *P–T* dependencies of Ti-in-quartz and Zr-in-sphene solubilities can be combined to obtain a crystallization pressure and temperature as long as a_{TiO_2} can be constrained (Hayden et al. 2007) and it can be assumed that both minerals equilibrated at the same conditions. Titanium activity for typical crustal rocks ranges between 0.5 and 1 (Ghent and Stout 1984). In a worst case with a_{TiO_2} unconstrained between these values the thermobarometer still yields useful information; the maximum differences in *P–T* returned from the combined thermobarometers will be $\sim 70°C$ and ~ 3 kbar.

Ti-in-quartz solubility can also be combined with an independent constraint on either *P* or *T* to obtain the crystallization temperature or pressure, respectively. Given a Ti-in-quartz concentration, a known *T* and values listed in

Table 2, the pressure can be determined by rearranging Eq. 9 to give,

$$P(kbar) = \frac{-a + bT + RT \ln a_{TiO_2} - RT \ln X^{Qtz}_{TiO_2}}{c}. \quad (11)$$

If temperature can be constrained to within ±25°C, the pressure can be estimated to within approximately ±1.2 kbar.

The temperature can be determined from a known *P* and a Ti-in-quartz concentration using

$$T(°C) = \frac{a + cP}{b - R \times \ln X^{Qtz}_{TiO_2} + R \times \ln a_{TiO_2}} - 273.15. \quad (12)$$

If pressure can be constrained to within ±1 kbar, the temperature can be estimated to within approximately ±20°C.

Ti-in-quartz solubility can also be used as a thermobarometer when combined with constraints imposed by phase equilibria, such as fluid inclusion isochoric data or well-constrained melt–solid phase relations (Fig. 8b; e.g., the water-saturated solidus for 'minimum' compositions).

At this time few published reports include measurements of Ti-in-quartz and Zr-in-rutile and/or Zr-in-sphene that can be used to test the reliability of using Ti-in-quartz solubility as a thermobarometer. Here we apply the new experimental results to modify previously interpreted crystallization conditions for quartz and rutile from blueschists of Sifnos, Greece (Spear et al. 2006), and quartz from the Bishop Tuff (Wark and Watson 2006; Wark et al. 2007).

Syros, Greece blueschists

The pressure dependence of the Ti-in-quartz thermometer makes it potentially an excellent barometer for blueschists, especially in rocks in which temperature can be constrained by independent means. For example, Spear et al. (2006) report on temperatures obtained from rutile crystals in blueschists from the island of Sifnos Greece, and analyses of quartz from these samples would enable determination of pressures of equilibration.

As an example of this application, Spear et al. (2005) reported preliminary data on both the Ti concentration in quartz and the Zr concentration in rutile from blueschists from the southern tip of the island of Syros, Greece. Ti concentrations in quartz were determined on the IMS 3f at Woods Hole Oceanographic Institute with an analytical precision of approximately ±0.1 ppm. Titanium concentrations in quartz range from 0.28 to 0.87 ppm. No systematic zoning was observed either in the analytical results or in CL images collected on samples. However, several grains showed slightly lower Ti values in the cores than at the rims (by 0.1–0.2 ppm). Quartz inclusions inside a large

garnet crystal have compositions in the middle of the total range ($\sim$0.35–0.5 ppm). Zr concentrations in rutile were measured on a Cameca SX-100 electron microprobe following the methods described by Spear et al. (2006) range from 25 to 50 ppm with counting precisions of $\sim$8 ppm.

Figure 9a shows a P–T diagram for samples from southern Syros with the range of Ti in quartz and Zr in rutile values plotted as isopleths. If it is assumed that both the quartz and the rutile crystals equilibrated at the peak of metamorphism, then the intersection of the isopleths can be used to infer average P–T conditions of around 22 $\pm$ 2.5 kbar and 560 $\pm$ 15°C, which is consistent with peak conditions inferred by Breecker (2001) for these rocks.
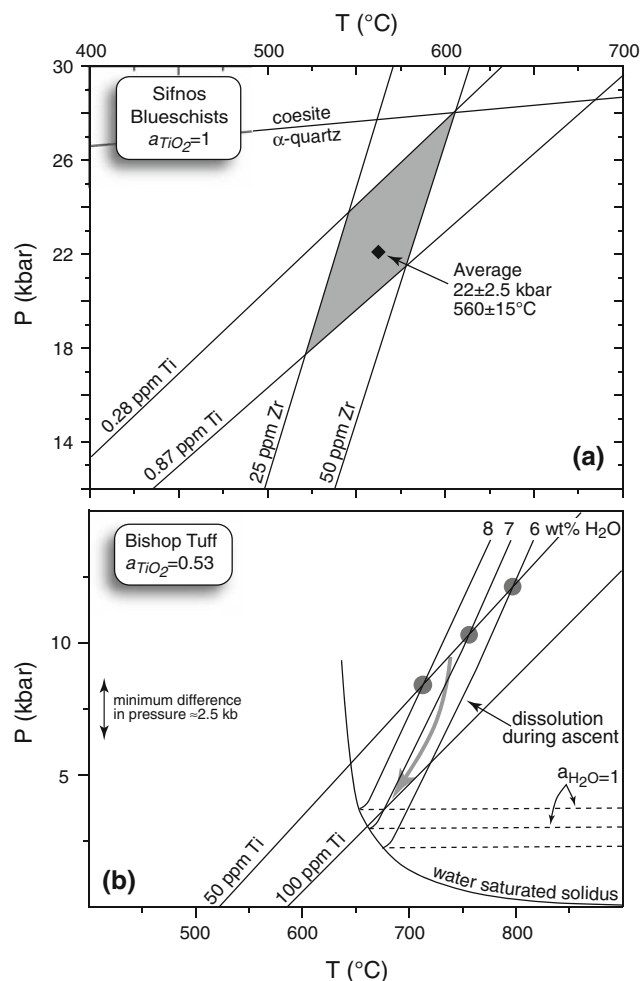

Fig. 9 a Simultaneous application of Ti-in-quartz and Zr-in-rutile solubility for usage as a thermobarometer to blueschists from Sifnos, Greece. See text for details. b P–T plot showing the 50 and 100 ppm Ti-in-quartz isopleths representative of the core and rim Ti contents of mid- to late-erupted Bishop Tuff. The cores and rims could have formed at any P–T along the respective isopleths. This means that the minimum P difference must have been $\sim$2.5 kbar between core and rim crystallization. If water contents and crystal contents during core and rim crystallization were known, P–T conditions of crystallization could be further constrained

Temperatures of blueschists are typically sufficiently low that diffusion of either Ti in quartz or Zr in rutile is minimal and the grains should preserve the composition from the time they were formed (e.g., Cherniak et al. 2007a, b). Any zoning observed should reflect growth zoning, similar to chemical zoning observed in low- to medium-grade garnets. However, by the mid-amphibolite facies, zoning of Ti in quartz may be substantially modified by diffusion (e.g., Spear and Wark 2009). This condition also requires that both quartz and rutile formed or recrystallized at the same P–T conditions if their simultaneous intersection is to be used to infer metamorphic conditions. As discussed by Spear et al. (2006), the reactions producing rutile in blueschists are not known, although the breakdown of ilmenite to rutile bearing assemblages typically occurs around 10 kbar. Quartz recrystallization may occur throughout the metamorphic history, as discussed by Spear and Wark (2009) and may show a progression of recrystallization as evidenced by chemical zoning. In short, there is no a priori reason to assume that quartz and rutile will equilibrate at the same metamorphic conditions, and careful application of these equilibria to metamorphic rocks requires a thorough evaluation of the reaction history.

The Bishop Tuff

Cathodoluminescence images of quartz crystals from the 0.76 Ma Bishop Tuff (eastern California, USA; Peppard et al. 2001; Hildreth and Wilson 2007) reveal that crystals from the early erupted units have fairly uniform CL patterns from core to rim; whereas, quartz crystals from mid- and late-erupted ignimbrites are strongly zoned with sharp boundaries separating dark CL cores from bright CL rims. Wark and Spear (2005) showed that differences in rim and core CL intensity are correlated with Ti contents. The original 10 kbar TitaniQ calibration was subsequently used to determine crystallization temperatures of $\sim$720°C ($\sim$50 ppm Ti) for quartz from early erupted units. The later erupted units contain quartz crystals with bimodal Ti concentrations. The 10 kbar TitaniQ calibration gave temperatures of $\sim$720°C for the dark CL cores with $\sim$50 ppm Ti and the bright CL rims with $\sim$100 ppm Ti yielded temperatures of $\sim$810°C (Wark and Watson 2006; Wark et al. 2007). Wallace et al. (1999) found that the melt inclusions hosted in the rims of quartz crystals contained higher concentrations of CO_2 and trace elements that are commonly associated with mafic magmas than the melt inclusions hosted in cores of quartz crystals. Anderson et al. (2000) suggested that the bright CL rims grew and trapped CO_2-rich melt inclusions as those quartz crystals sank into hotter and less evolved regions of a compositionally and thermally stratified magma system.

The quartz crystals with bimodal Ti contents have dark CL cores with truncated oscillatory zones indicating that the crystals underwent partial dissolution prior to growth of the bright CL rims. Wark et al. (2007) argued against the crystal sinking model of Anderson et al. (2000) because the quartz crystals did not show a gradual rimward change in CL intensity (i.e., Ti content) as would be expected for slow crystal sinking. Wark et al. (2007) interpreted the CL patterns, Ti contents and CO_2/trace element contents of melt inclusions as reflecting an increase in temperature that was caused by injection of hot mafic magma into deeper parts of the Bishop system. They suggested that quartz was able to grow at higher temperatures, instead of dissolving, because injection of CO_2-rich magma decreased water activity and raised the solidus temperature.

The new experimental results demonstrating a strong pressure effect on Ti-in-quartz solubility can be used to modify previous interpretations of Wark et al. (2007) that were based on the 10 kbar TitaniQ calibration (Wark and Watson 2006). On Fig. 9b the 50 and 100 ppm Ti-in-quartz isopleths ($a_{TiO_2} \approx 0.53$; Reid et al. submitted), corresponding to the average Ti contents of the dark CL cores and bright rims of later erupted Bishop Tuff quartz crystals, are shown along with the water-saturated solidus for 'minimum' compositions (Holtz and Johannes 1994). The quartz cores must have formed along the 50 ppm Ti isopleth and quartz rims must have formed along the 100 ppm isopleth.

Crystallization of rhyolitic compositions are typified by early quartz crystallization along a liquidus line, which is defined by the water content of the system, followed by K-feldspar and plagioclase with final crystallization occurring on the water-saturated solidus. Titanium activity of the Bishop system is assumed to have been buffered at $a_{TiO_2} = 0.53$ by the presence of Fe–Ti oxides during quartz crystallization (activity calculated using Fe–Ti oxides of Hildreth and Wilson 2007; see Reid et al. submitted). The cores and rims could have formed at any P–T condition along the respective isopleths, which means that the minimum difference in pressure must have been at least ~ 2.5 kbar between core and rim crystallization (Fig. 9b).

If water and crystal contents of the melt during times of quartz core and rim crystallization were known, then the P–T conditions of quartz crystallization could be estimated. Given this information, the Ti-in-quartz contents of the quartz crystals could be used to construct an ascent trajectory for the magma that ultimately carried the quartz crystals to the surface. For example, if the system contained 3.5 wt% H_2O and was 50% solidified (anhydrous minerals) during crystallization of the dark CL cores, then the P–T estimate for crystallization would be constrained by the intersection of the 7 wt% liquidus with the 50 ppm Ti-in-quartz isopleth at ~ 10 kbar and

$\sim 760°C$. Higher water contents in the magmatic system would return lower pressures for the isopleth-liquidus intersection (see 8 wt% liquidus in Fig. 9b). Adiabatic ascent of the magma to lower pressures along *any* trajectory steeper than the liquidus lines would have caused dissolution of quartz crystals (Fig. 9b; cf. Holtz and Johannes 1994) similar to patterns observed in quartz crystals from the late-erupted Bishop Tuff units. During ascent along an adiabatic trajectory the water activity of the melt and the percentage of melt present would have continually increased as the water-saturated solidus was approached.

The *minimum P–T* conditions for crystallization of the bright CL rims can be constrained by the 100 ppm Ti-in-quartz isopleth and the water-saturated solidus. The 100 ppm Ti isopleth crosses the water-saturated solidus just below the 7 wt% H_2O liquidus at $\sim 660°C$ and ~ 3 kbar, P–T conditions that are consistent with most previous interpretations for the depth and temperature of final crystallization just prior to eruption of the Bishop Tuff magma system (e.g., Hildreth and Wilson 2007; Ghisoro and Evans 2008). Assuming lower initial water contents would place the depth of core and rim crystallization at higher pressures (Fig. 9b) at the intersection of respective isopleths with lower water content liquidus lines. Regardless of assumed water and crystal content present during quartz crystallization, it is clear that the dark CL cores of crystals must have crystallized at higher pressure than the bright CL rims because adiabatic ascent trajectories cannot have negative dP/dT.

The P–T dependencies of Ti-in-quartz solubility provide additional details regarding magmatic evolution of the Bishop magmatic system that could not be extracted by applying a simple geothermometer. The presence of dark CL cores overgrown by bright CL rims in quartz crystals from the Bishop Tuff and other rhyolites (e.g., Katmai) apparently reflects a common emplacement and eruption process that likely operates in many silicic magmatic systems. Hildreth and Wilson (2007) suggest that large-scale rhyolitic systems like the Bishop are characterized by crystal-poor upper-crustal magma chambers that grade down into quartzo-feldspathic crystal mush zones extending from mid- to lower-crustal regions. Mafic magma supplied to the deepest regions maintains the magmatic system over millions of years. Batches of silicic magma are incrementally supplied from deeper levels and assembled piecemeal into the upper-crustal magma chamber. It is plausible that the dark CL cores of quartz crystals grew in a deep-crustal crystal mush root zone at pressures greater than the final emplacement level, followed by entrainment during emplacement of a batch of magma to an upper-crustal reservoir where the bright CL rim grew at ~ 3 kbar. The truncated CL zones of the quartz cores suggest that

dissolution occurred during ascent of the magma as would be expected during adiabatic ascent (Fig. 9b; Holtz and Johannes 1994). Mafic input is not necessarily required for dissolution of quartz crystals. The new experimental results and the model of Hildreth and Wilson (2007) provide a consistent framework to describe the bimodal Ti distribution and truncated CL patterns in quartz crystals from the later erupted Bishop Tuff. This example using the Bishop Tuff demonstrates how Ti-in-quartz solubility can be used as a thermobarometer when it is combined with phase equilibria of silicic magmas.

Concluding remarks

The experimental results presented here showing the strong P–T dependence of Ti-in-quartz solubility will likely have significant implications for thermobarometry of crustal rocks from igneous, metamorphic and hydrothermal environments. XANES spectra demonstrate that over the range of pressures investigated here Ti^{4+} substitutes on the fourfold Si^{4+} site in quartz. Thus, the experimental results were fit to a simple solubility model that can be used to predict Ti-in-quartz solubility up to ~ 20 kbar, which is the maximum pressure investigated here. As long as titanium activity can be constrained, the P–T dependencies of Ti-in-quartz solubility can be used as a thermobarometer when used in combination with another thermobarometer in a coexisting mineral or an independent P or T estimate of quartz crystallization.

We expect that Ti-in-quartz thermobarometry will find widespread application to metamorphic rocks that contain rutile through simultaneous application of the Ti-in-quartz and Zr-in-rutile solubilities to obtain a unique P–T estimate for quartz and rutile co-crystallization. Although quartz-bearing igneous rocks typically lack rutile, sphene is a common accessory mineral. In such rocks, Ti-in-quartz and Zr-in-sphene solubilities can be used for thermobarometry. A potentially elegant usage of Ti-in-quartz solubility as a thermobarometer will be to combine Ti-in-quartz solubility with fluid inclusion microthermometry. Such applications could be especially useful for felsic igneous rocks crystallized near the water-saturated solidus that lack either rutile or sphene. The crossing point of fluid inclusion isochores with Ti-in-quartz isopleths will yield a P–T estimate of quartz crystallization and fluid entrapment. Since quartz oftentimes preserves deformation fabrics, Ti-in-quartz thermobarometry may also reveal P–T conditions of deformation, recrystallization and fabric formation in cataclystic rocks. As with all thermobarometric methods, combining mineral equilibria requires some insurance that the paired phases were in equilibrium during crystallization and that later alteration has not affected their compositions.

Given these precautions, Ti-in-quartz should prove valuable for thermobarometry across a wide spectrum of geologic conditions.

Appendix

The equation to convert Ti (ppm) to mole fraction TiO_2 in quartz ($X_{TiO_2}^{quartz}$) is

$$X_{TiO_2}^{quartz} = \frac{\frac{Ti(ppm)}{1E4 \times 0.599 \times 79.87}}{\frac{Ti(ppm)}{1E4 \times 0.599 \times 79.87} + \left[\left(100 - \frac{Ti(ppm)}{1E4 \times 0.599 \times 79.87} \right) \times \frac{1}{60.09} \right]}.$$

The equation to convert Zr (ppm) to mole fraction ZrO_2 in rutile ($X_{ZrO_2}^{rutile}$) is

$$X_{ZrO_2}^{rutile} = \frac{\frac{Zr(ppm)}{1E4 \times 0.74 \times 123.22}}{\frac{Zr(ppm)}{1E4 \times 0.74 \times 123.22} + \left[\left(100 - \frac{Zr(ppm)}{1E4 \times 0.74 \times 123.22} \right) \times \frac{1}{79.87} \right]}.$$

The equation to convert Zr (ppm) to mole fraction ZrO_2 in sphene ($X_{ZrO_2}^{sphene}$) is

$$X_{ZrO_2}^{sphene} = \frac{\frac{Zr(ppm)}{1E4 \times 0.74 \times 123.22}}{\frac{Zr(ppm)}{1E4 \times 0.74 \times 123.22} + \left[\left(100 - \frac{Zr(ppm)}{1E4 \times 0.74 \times 123.22} \right) \times \frac{1}{196.03} \right]}.$$

References

Anderson AT Jr, Crewe AV, Goldsmith JR, Moore PB, Newton RC, Olsen EJ, Smith JV, Wyllie PJ (1970) Petrologic history of Moon suggested by petrography, mineralogy, and crystallography. Science 167:587–590

Anderson AT Jr, Davis AM, Lu F (2000) Evolution of bishop tuff rhyolitic magma based on melt and magnetite inclusions and zoned phenocrysts. J Petrol 41:449–473

Andreoni W, Curioni A (2000) New advances in chemistry and materials science with CPMD and parallel computing. Parallel Comput 26:819–842

Bair RA, Goddard WA (1980) Ab initio studies of the X-ray absorption edge in copper complexes. l. Atomic Cu^{2+} and $Cu(II)Cl_2$. Phys Rev B 22:2767–2776

Bekas C, Curioni A (2008) Atomic wavefunction initialization in ab initio molecular dynamics using distributed Lanczos. Parallel Comput 34:441–450

Berry AJ, Walker AM, Hermann J, HStC O'Neill, Foran GF, Gale JD (2007) Titanium substitution in forsterite. Chem Geol 242:176–186

Breecker DA (2001) Mineral assemblages in high-pressure quartz-mica schists from Syros, Cyclades, Greece. Unpublished BA Thesis, Amherst College, p 70

Cherniak DJ (2006) Zr diffusion in titanite. Contrib Mineral Petrol 152:639–647

Cherniak DJ, Watson EB, Wark DA (2007a) Ti diffusion in quartz. Chem Geol 236:65–74

Cherniak DJ, Manchester J, Watson EB (2007b) Zr and Hf diffusion in rutile. Earth Planet Sci Lett 261:267–279

Denen WH (1964) Impurities in quartz. Geol Soc Am Bull 75:241–246

Denen WH (1966) Stoichiometric substitution in natural quartz. Geochim Cosmochim Acta 30:1235–1241

Farges F (1997) Coordination of Ti^{4+} in silicate glasses: a high-resolution XANES spectroscopy study of the Ti K edge. Am Mineral 82:36–43

Farges F, Brown GE Jr, Rehr JJ (1996a) Coordination chemistry of Ti(IV) in silicate glasses and melts: I. XAFS study of titanium coordination in oxide compounds. Geochim Cosmochim Acta 60:3023–3038

Farges F, Brown GE Jr, Rehr JJ (1996b) Coordination chemistry of Ti(IV) in silicate glasses and melts: II. Glasses at ambient temperature and pressure. Geochim Cosmochim Acta 60:3039–3053

Farges F, Brown GE Jr, Rehr JJ (1997) Ti K-edge XANES studies of Ti coordination and disorder in model compounds: comparison between theory and experiment. Phys Rev B 56:1809–1819

Ferris EDA, Essene EJ, Becker U (2008) Computational study of the effect of pressure on the Ti-in-zircon geothermometer. Eur J Mineral 20:745–755

Ferry JM, Watson EB (2007) New thermodynamic models and revised calibrations for the Ti-in-zircon and Zr-in-rutile thermometers. Contrib Mineral Petrol 154:429–437

Ghent ED, Stout MZ (1984) TiO_2 activity in metamorphosed pelitic and basic rocks: principles and applications to metamorphism in southeastern Canadian Cordillera. Contrib Mineral Petrol 86:248–255

Ghisoro MS, Evans BW (2008) Thermodynamics of rhombohedral oxide solid solutions and a revision of the Fe-Ti two-oxide geothermometer and oxygen-barometer. Am J Sci 308:957–1039

Hayden LA, Watson EB, Wark DA (2007) A thermobarometer for sphene (titanite). Contrib Mineral Petrol 155:529–540

Hildreth W, Wilson CJN (2007) Compositional zoning of the bishop tuff. J Petrol 48:951–999

Holtz F, Johannes W (1994) Maximum and minimum water contents of granitic melts: implications for chemical and physical properties of ascending magmas. Lithos 32:149–159

Kennedy GC, Wasserburg GJ, Heard HC, Newton RC (1962) The upper three-phase region in the SiO2–H2O system. Am J Sci 260:501–521

Kresse G, Furthmuller J (1996) Efficiency of ab initio total energy calculations for metals and semiconductors using a plane-wave basis set. Computat Mat Sci 6:15–50

Landtwing M, Petke T (2005) Relationships between SEM-cathodoluminescence response and trace element composition of hydrothermal vein quartz. Am Mineral 90:122–131

Levien L, Prewitt CT, Weidner DJ (1980) Structure and elastic properties of quartz at pressure. Am Mineral 65:920–930

Lowers HA, Rusk BG, Koenig A (2007) Application of the titaniq geothermometer to hydrothermal quartz. GSA Denver Annual Meeting abstract, pp 226–229

Moneke T, Kempe U, Götze J (2002) Genetic significance of trace element content in metamorphic and hysrothermal quartz: a reconnaissance study. Earth Planet Sci Lett 202:709–724

Müller A, Wiedenbeck M, Van den Kerkhof AM, Kronz A, Simon K (2003) Trace elements in quartz-A combined electron microprobe, secondary ion mass spectrometry, laser ablation ICPMS and cathodoluminescence study. Eur J Mineral 15:747–763

Ostapenko GT, Gamarnik MY, Gorogotskaya LI, Kuznetsov GV, Tarashchan AN, Timoshkova LP (1987) Isomorphism of titanium substitution for silicon in quartz: experimental data. Mineral Zh 9:30–40

Ostapenko GT, Tarashchan AN, Mitsyuk BM (2007) Rutile-quartz geothermobarometer. Geochem Int 45:506–508

Paier J, Hirschl R, Marsman M, Kresse G (2005) The Perdew–Burke–Ernzerhof exchange-correlation functional applied to the G2–1 test set using a plane-wave basis set. J Chem Phys 122:234102

Peppard BT, Steele IM, Davis AM, Wallace PJ, Anderson AT (2001) Zoned quartz phenocrysts from the rhyolitic bishop tuff. Am Mineral 86:1034–1052

Perdew JP, Burke K, Ernzerhof M (1996) Generalized gradient approximation made simple. Phys Rev Lett 77:3865–3868

Philpotts AR (1990) Principles of igneous and metamorphic petrology. Prentice Hall, Englewood Cliffs

Ravel B, Newville M (2005) ATHENA, ARTEMIS, HEPHAESTUS: data analysis for X-ray absorption spectroscopy using IFEFFIT. J Synchrotron Radiat 12:537–541

Reid MR, Vazquez JA, Schmitt AK (2010) Zircon-scale insights into the history of a supervolcano, Bishop Tuff, Long Valley, California—with implications for the Ti-in-zircon geothermometer. Contrib Mineral Petrol (accepted)

Rusk BG, Reed MH, Dilles JH, Kent AJR (2006) Intensity of quartz cathodoluminescence and trace-element content in quartz from the porphyry copper deposit at Butte, Montana. Am Mineral 91:1300–1312

Shen AH, Bassett WA, Chou I-M (1993) The α-β quartz transition at high temperatures and pressures in a diamond anvil cell by laser interferometry. Am Mineral 78:694–698

Spear FS (1993) Metamorphic phase equilibria and pressure-temperature-time paths. Mineralogical Society of America, Washington

Spear FS, Wark DA (2009) Cathodoluminescence imaging and titanium thermometry metamorphic quartz. J Metamorph Geol 27:187–205

Spear FS, Cheney JT, Wark DA (2005) Application of accessory phase/trace element thermometry to blueschists from Syros and Sifnos, Greece. Geochim Cosmochim Acta 69 (Goldschmidt Conf Abstr):A25

Spear FS, Wark DA, Cheney JT, Schumaker JC, Watson EB (2006) Zr-in-rutile thermometry in blueschists from Sifnos, Greece. Contrib Mineral Petrol 152:375–385

Sprunt ES (1981) Causes of quartz cathodoluminescence colors. Scan Electron Microsc 1981:525–535

Suttner LJ, Leininger RK (1972) Comparison of trace element content of plutonic, volcanic and metamorphic quartz from southwestern Montana. Bull Geol Soc Am 83:1855–1862

Tailby ND, Walker AM, Berry AJ, Hermann J, Evans KA, Mavrogenes JA, O'Neill H St C, Rodina IS, Soldatov AV, Rubatto D, Sutton SR (2010) Ti site occupancy in zircon. Geochim Cosmochim Acta (in press)

Tomkins HS, Powell R, Ellis DJ (2007) The pressure dependence of the zirconium-in-rutile thermometer. J Metamorph Geol 25:703–713

Troullier N, Martins JL (1991) Efficient pseudopotentials for plane-wave calculations. II. Operators for fast iterative diagonalization. Phys Rev B Cond Matter 43:8861

Wallace P, Anderson AT, Davis AM (1999) Gradients in H20, CO2, and exsolved gas in a large-volume silicic magma system: interpreting the record preserved in melt inclusions from the Bishop Tuff. J Geophys Res 104:20097–20122

Wark DA, Spear FS (2005) Titanium in quartz: cathodoluminescence and thermometry. Geochim Cosmochim Acta 69:A592

Wark DA, Watson EB (2006) The TitaniQ: a Titanium-in-quartz geothermometer. Contrib Mineral Petrol 152:743–754

Wark DA, Hildreth W, Spear FS, Cherniak DJ, Watson EB (2007) Pre-eruption recharge of the bishop magma system. Geology 35:235–238

Watson EB, Wark DA, Price JD, Van Orman JA (2002) Mapping the thermal structure of solid-media pressure assemeblies. Contrib Mineral Petrol 142:640–652

Watson EB, Wark DA, Thomas JB (2006) Crystallization thermometers for zircon and rutile. Contrib Mineral Petrol 151:413–433

Waychunas GA (1987) Synchrotron radiation XANES spectroscopy of Ti in minerals: effects of Ti bonding distances, Ti valence, and site geometry on absorption edge structure. Am Mineral 72:89–101

Wiebe RA, Wark DA, Hawkins DP (2007) Insights from quartz cathodoluminescence zoninginto crystallization of the Vinalha-ven granite, coastal Maine. Contrib Mineral Petrol 154:439–453

Zicovich-Wilson CM, Pascale F, Roetti C, Saunders VR, Orlando R, Dovesi R (2004) Calculation of the vibration frequencies of α-quartz: the effect of Hamiltonian and basis set. J Computat Chem 25:15